Electrical Power and Energy Systems 106 (2019) 455–466

Contents lists available at ScienceDirect

Electrical Power and Energy Systems

journal homepage: www.elsevier.com/locate/ijepes

Designing SSSC, TCSC, and STATCOM controllers using AVURPSO, GSA, and GA for transient stability improvement of a multi-machine power system with PV and wind farms

Amir Movahedi[a], Abolfazl Halvaei Niasar[a], G.B. Gharehpetian[b]

[a] Faculty of Electrical and Computer Engineering, University of Kashan, Kashan, Iran
[b] Electrical Engineering Department, Amirkabir University of Technology, Tehran, Iran

ARTICLE INFO

Keywords:
PV
DFIG
LVRT
FACTS
PSS
AVURPSO

ABSTRACT

In this paper, the effects of three FACTS controllers, static synchronous series compensator (SSSC), thyristor-controlled series compensator (TCSC), and static synchronous compensator (STATCOM), on the transient stability of a multi-machine power system in the presence of two 200 MW wind farms based on a doubly fed induction generator (DFIG) and a 120 MW photovoltaic (PV) solar plant are studied. Also, power system stabilizers (PSSs) are installed on four synchronous machines. It is generally accepted that there is a threat to the stability of power systems with the penetration of wind farm and PV plant. Therefore, in order to improve transient stability in the power system, this paper proposes the application of PI controllers in PV and wind farm controllers and a combination of PSS and FACTS controllers, whose coordination is very important. The design problems of the PSS, FACTS, and PI controllers are formulated as an optimization problem, and the adaptive velocity update relaxation particle swarm optimization (AVURPSO) algorithm, gravitational search algorithm (GSA), and genetic algorithm (GA) are employed to search for the optimal controller parameters. These three approaches identify the solution to a given objective function, but they employ different strategies and computational efforts. Therefore, a comparison of their performance is required.

1. Introduction

Considerable effort has been made for the integration of renewable energies into the grid in order to meet the imperative demand of a clean and reliable electricity generation [1]. The main purpose of this paper is to apply a PV solar plant, wind farms, and synchronous machines simultaneously in the power system. In this case, grid stability and robustness may be violated due to the intermittency and interaction of solar and wind renewables. Related grid demands have been presented, in which case far more attention should be paid to specific requirements, like low voltage ride-through (LVRT) and reactive power injection capability [2–5].

Due to the declined PV cell price and advanced power electronics technology, the penetration level will become much higher. A sudden stoppage of all grid-connected PV systems in an unintentional islanding operation mode may trigger much more severe grid problems than the initial event, e.g. power outages and voltage flickers. In order to solve potential issues, several European countries have updated the grid codes for voltage systems [6–8].

On the other hand, the share of wind power with respect to total installed power capacity is increasing worldwide. Currently, DFIG is the most frequently used generator for wind turbines (WTs) due to its advantages [9–12]. The stator of the DFIG is directly connected to the grid while its rotor is connected through an AC/DC/AC converter. When the grid voltage dip occurs, the stator flux cannot be changed and, therefore, stator windings will induce a DC component of the stator flux which also contains a negative-sequence component during asymmetrical grid voltage dips.

Since the capacity of the DFIG converter is only 25–30% [10,11], the grid fault can easily cause rotor overvoltage or over-current, which makes the converter a direct threat to the safety of the WT operation. Consequently, an effective control should be exerted in order to prevent stator and rotor inrush currents as well as overvoltage and torque oscillations, and to allow the DFIG-based WT to remain connected to the grid during faults. The proposed solution involves the use of PI controllers in rotor-side and grid-side controllers and application of FACTS devices on the transmission line.

Flexible AC transmission system (FACTS) devices can be used to control power flow and enhance system stability [13–16]. This paper investigates the improvement of the transient stability of a two-area

E-mail addresses: a.movahedi@grad.kashanu.ac.ir (A. Movahedi), halvaei@kashanu.ac.ir (A.H. Niasar), grptian@aut.ac.ir (G.B. Gharehpetian).

https://doi.org/10.1016/j.ijepes.2018.10.019
Received 4 December 2017; Received in revised form 9 October 2018; Accepted 16 October 2018

power system with PV and wind farms, using an SSSC, TCSC, and STATCOM.

SSSC is utilized for power flow control, voltage stability, and phase-angle stability. The benefit of SSSC over conventional controllable series capacitors is that SSSC induces both capacitive and inductive series compensating voltages on a line [17–19]. TCSC is a typical series FACTS device employed to vary the reactance of the transmission line [20,21]. STATCOM can be defined as a synchronous static generator which operates as a shuntly-connected reactive power static compensator. Its output current can be fully controlled in both the capacitive and inductive range, independently of AC network voltage [22,23].

An electronic device used to improve the stability of the power system is called power system stabilizer (PSS). PSSs which are excitation system-based damping controllers were widely used in the past to add damping torque and increase the damping of these oscillations [24,25]. This paper contains a coordinated simulink model of PSS and different types of FACTS devices for two area power systems and examines three-phase fault conditions with and without controllers.

Numerous studies have been conducted in the field of simultaneous coordinated design of PSS and FACTS controllers [25,26]. In [27], the brainstorm optimization algorithm (BSOA) has been employed to find the optimal location and setting of TCSC and SVC controllers. Moreover, in [28], a damping controller of the SVC has been designed using the adaptive-network-based fuzzy inference system (ANFIS). Furthermore, the optimal placement problems of multiple UPFC solved by gravitational search algorithm (GSA) has been presented in [29].

Several modern heuristic tools that facilitate the solution of optimization problems which were previously difficult or impossible to address have evolved in the last two decades. These tools include, among others, evolutionary computation, simulated annealing, tabu search, and particle swarm. The genetic algorithm (GA), gravitational search algorithm (GSA), and particle swarm optimization (PSO) techniques emerged as promising algorithms for handling optimization problems. These techniques are gaining popularity within the research community as design tools and problem-solvers because of their versatility and capability for optimization in complex multimodal search spaces applied to non-differentiable cost functions.

UPFC location and its control parameters have been optimized using GA presented in [30]. In [31], the GA scheme determined the optimal location for the UPFC while tuning its control parameters and locations of the PSS under different operating conditions.

In addition, [32] presents the application of an improved PSO algorithm for the optimal sizing and allocation of a STATCOM and minimization of voltage deviations at all the buses in a power system. Also, individual designs of UPFC controllers and PSS using PSO technique have been discussed in [33].

The proposes of GSA for the optimal designing of SSSC controller were presented in [34] and the optimum coordination of FACTS devices solved by GSA were given in [35].

The novelty of the present study is finding the global optimum of the spread factor parameter at the upper level using an adaptive velocity update PSO, namely AVURPSO, that has a higher convergence speed and accurate response than the PSO algorithm [36,37]. In this paper, three methods of AVURPSO, GSA, and GA are used to design and optimize the parameters of PSS, FACTS, and PI controllers.

2. FACTS devises

2.1. Static synchronous series compensator

SSSC is an example of a FACTS device whose primary function is to change the characteristic impedance of the transmission line and thus change the power flow. The impedance of the transmission line is changed by injecting a voltage which leads or lags the transmission line current by 90°. If the SSSC is equipped with an energy storage system, the SSSC receives the added advantage of real and reactive power compensation in the power system [17,19]. By controlling the angular position of the injected voltage with respect to the line current, the real power is provided by the SSSC with the energy storage element.

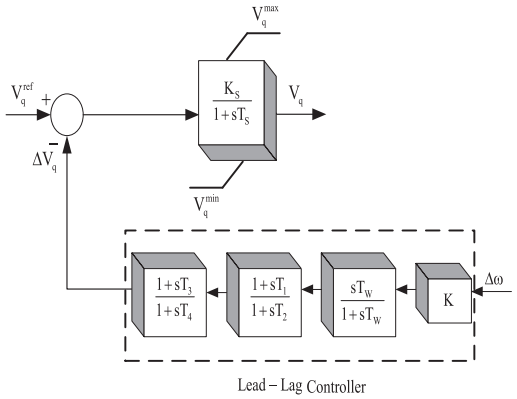

(a). SSSC with lead-lag controller

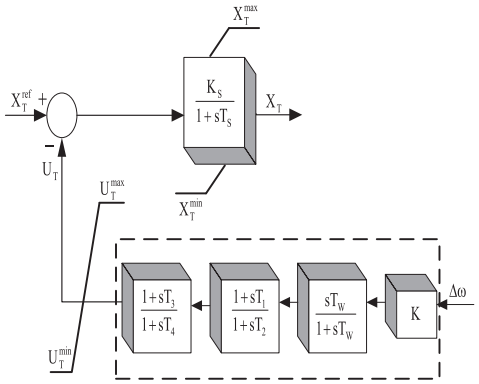

(b). TCSC with lead-lag controller

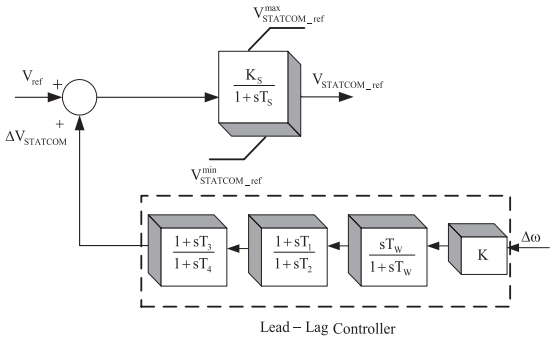

(c). STATCOM with lead-lag controller

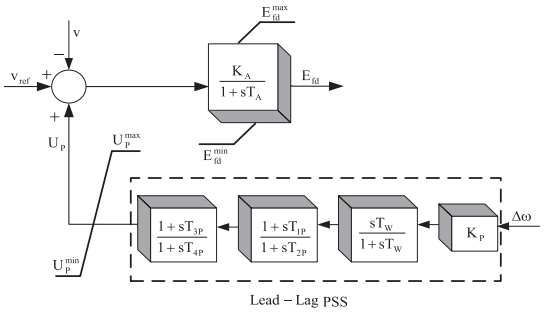

(d). IEEE type-ST1 excitation system with PSS

Fig. 1. Lead-lag controller.

The SSSC-damping controller structure is illustrated in Fig. 1a. The speed deviation Δω is considered as the input to the damping controller. The lead-lag block containing the stabilizer gain block determines the amount of damping. Next, the washout sub-block is used to reduce the over-response of damping during severe events and serves as a high-pass filter with a time constant that allows the signal associated with oscillations in the rotor speed to pass unchanged. Without this block, steady-state changes would modify the terminal voltages. Finally, the time constants of the phase compensator block are chosen such that the phase lag/lead of the system is fully compensated. In Fig. 1a, K and time constants T_1, T_2, T_3, and T_4 can be calculated using AVURPSO, GSA, and GA.

2.2. Thyristor controlled series compensator

TCSC is connected in series with transmission lines to compensate for the inductive reactance of the line, increase the maximum transmittable power and decrease the effective reactive power loss. The complete TCSC controller structure is shown in Fig. 1b. The output signal of the TCSC is the desired capacitive/inductive compensation signal, noted as X_{TCSC} [20]. In Fig. 1b, K_T and time constants T_1, T_2, T_3, and T_4 can be calculated using AVURPSO, GSA, and GA. The reactance of TCSC is expressed as follows:

$$\dot{X}_T = [-X_T + K_S(X_T^{ref} - U_T)]/T_S \tag{1}$$

2.3. Static synchronous compensator

STATCOM in a steady-state operating regime which replicates the operating characteristics of a rotating synchronous compensator. The basic electronic block of a STATCOM is a voltage-sourced converter that converts a DC voltage at its input terminals into a three-phase set of AC voltages at a fundamental frequency with a controllable magnitude and phase angle [22,23]. A STATCOM can be used for voltage regulation in a power system, having as an ultimate goal an increase in transmittable power as well as improvements of steady-state transmission characteristics and the overall stability of the system.

The commonly used lead–lag structure depicted in Fig. 1c is chosen in this study as a STATCOM-based damping controller. K and time constants T_1, T_2, T_3, and T_4 can be calculated using AVURPSO, GSA, and GA. In Fig. 1c, V_{ref} represents the reference voltage as desired by the steady operation of the system.

3. Power system stabilizer and system model

In this study, all synchronous generators are equipped with PSSs. The generator is represented by the third-order model consisting of the following swing equations [24,25]:

$$\dot{\delta} = \omega_b(\omega - 1) \tag{2}$$

$$\dot{\omega} = [P_m - P_e - D(\omega - 1)]/M \tag{3}$$

where P_e and P_m are the output and input powers of the generator, and ω and δ are the speed and rotor angle, respectively. The internal voltage is given by:

$$\dot{E}_q' = [-E_q' - (x_d - x_d')i_d + E_{fd}]/T_{d0}' \tag{4}$$

The real power output of the generator is described as:

$$P_e = v_d i_d + v_q i_q \tag{5}$$

The excitation system can be represented by the IEEE type-ST1 system demonstrated in Fig. 1d and described by [28]:

$$\dot{E}_{fd} = [-E_{fd} + K_A(V_{ref} - v + U_{PSS})]/T_A \tag{6}$$

The time constants T_{1P}, T_{2P}, T_{3P}, T_{4P}, and K_P are calculated using AVURPSO, GSA, and GA.

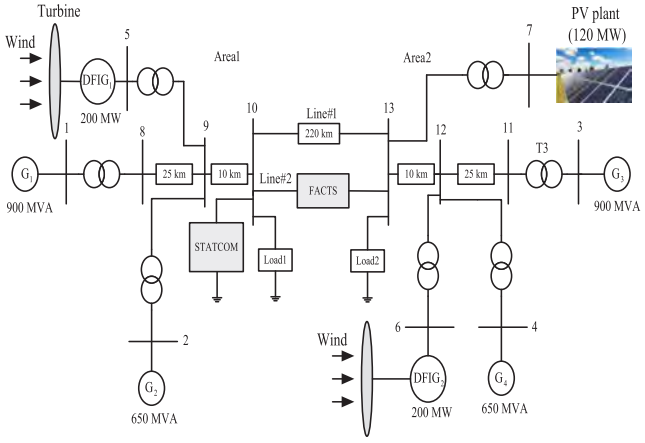

Fig. 2. Power system with PV and wind farms.

Fig. 2 illustrates the structure of the proposed system [38]. In Fig. 2, the power system consists of different areas: Two synchronous generators G_1 and G_2 and a wind farm based on $DFIG_1$ are in the first area, while G_3, G_4, $DFIG_2$ and PV plant are in the second area. G_1 and G_3 are 900 MVA; G_2 and G_4 are 650 MVA; $DFIG_1$ and $DFIG_2$ are 200 MW; and PV plant is 120 MW. SSSC and TCSC in the second line are between bus 10 and bus 13 (in FACTS block), and STATCOM is connected in bus 10. Moreover, PSS is installed on four synchronous generators (G_1, G_2, G_3, and G_4). Finally, the first and second areas are connected by two 230 kV transmission lines and a length of 220 km.

3.1. Wind farm

The wind farm basically consists of DFIG, a wind turbine with a drive train system, RSC, GSC, DC-link capacitor, pitch controller, coupling transformer, and protection system as shown in Fig. 3 [9,11].

The wind turbine with the DFIG system is an induction-type generator in which the stator windings are directly connected to the three-phase grid, and the rotor windings are fed through three-phase back-to back insulated-gate bipolar transistor (IGBT)-based pulse width modulation (PWM) converters. The dynamics of the DFIG is represented by a fourth-order state-space model using the synchronously rotating reference frame (qd-frame) as given in (7)–(10) [9–11]:

$$V_{qs} = r_s I_{qs} + \omega_e \lambda_{ds} + \frac{d\lambda_{qs}}{dt} \tag{7}$$

$$V_{ds} = r_s I_{ds} - \omega_e \lambda_{qs} + \frac{d\lambda_{ds}}{dt} \tag{8}$$

$$V_{qr} = r_r I_{qr} + (\omega_e - \omega_r)\lambda_{dr} + \frac{d\lambda_{qr}}{dt} \tag{9}$$

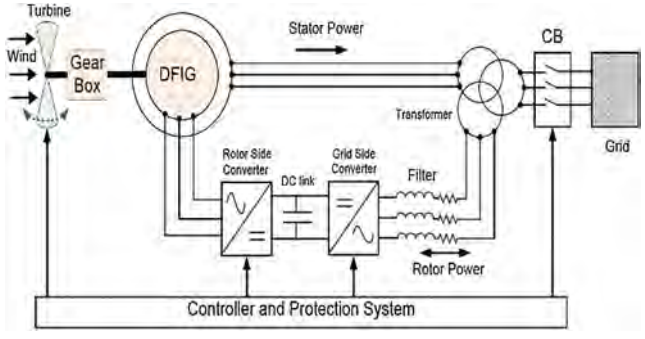

Fig. 3. Schematic diagram of DFIG wind turbine system.

$$V_{dr} = r_r I_{dr} + (\omega_e - \omega_r)\lambda_{qr} + \frac{d\lambda_{dr}}{dt} \tag{10}$$

where V_{qs}, V_{ds}, V_{qr}, and V_{dr} are the q- and d-axis stator and rotor voltages, respectively; I_{qs}, I_{ds}, I_{qr}, and I_{dr} are the q- and d-axis stator and rotor currents, respectively; λ_{qs}, λ_{ds}, λ_{qr} and λ_{dr} are the q- and d-axis stator and rotor fluxes, respectively; ω_e is the angular velocity of the synchronously rotating reference frame; ω_r is rotor angular velocity; and r_s and r_r are the stator and rotor resistances, respectively. The flux linkage equations are given as:

$$\lambda_{qs} = L_s I_{qs} + L_m I_{qr} \tag{11}$$

$$\lambda_{ds} = L_s I_{ds} + L_m I_{dr} \tag{12}$$

$$\lambda_{qr} = L_m I_{qs} + L_r I_{qr} \tag{13}$$

$$\lambda_{dr} = L_m I_{ds} + L_r I_{dr} \tag{14}$$

where L_s, L_r, and L_m represents the stator, rotor, and mutual inductances, respectively. Assuming negligible power losses in stator and rotor resistances, the active and reactive power outputs from stator and rotor sides are given as:

$$P_s = -\frac{3}{2}(V_{qs} I_{qs} + V_{ds} I_{ds}) \tag{15}$$

$$Q_s = -\frac{3}{2}(V_{qs} I_{ds} - V_{ds} I_{qs}) \tag{16}$$

$$P_r = -\frac{3}{2}(V_{qr} I_{qr} + V_{dr} I_{dr}) \tag{17}$$

$$Q_r = -\frac{3}{2}(V_{qr} I_{dr} - V_{dr} I_{qr}) \tag{18}$$

The total active and reactive power generated by DFIG is:

$$P_{Total} = P_s + P_r \tag{19}$$

$$Q_{Total} = Q_s + Q_r \tag{20}$$

If P_{Total} and/or Q_{Total} is positive, DFIG is supplying power to the power grid; otherwise, it is drawing power from the grid. T_e is the electromagnetic torque generated by the machine, which can be written in terms of flux linkages and currents as follows:

$$T_e = \frac{3}{2}(\lambda_{qs} I_{ds} - \lambda_{ds} I_{qs}) \tag{21}$$

where positive (negative) values of T_e mean DFIG works as a generator (motor).

3.1.1. Control systems

The typical structure of a PI control system is shown in Fig. 4a [9–11], where the error signal e(t) is used to generate the proportional and integral actions, with the resulting signals weighted and summed to form the control signal u(t) applied to the plant model. A mathematical description of the PI controller is:

$$u(t) = K_P e(t) + K_i \int_0^t e(\tau) d\tau = u_p(t) + u_i(t) \tag{22}$$

where u(t) indicates the input signal to the plant model, the error signal e(t) is defined as e(t) = r(t)-y(t), and r(t) denotes the reference input signal. In this paper, AVURPSO, GSA, and GA are employed to design and optimize the parameters of PI controllers.

The rotor-side converter (RSC) is applied to control the wind turbine output power and the voltage or reactive power measured at grid terminals. Power is controlled in order to follow a pre-defined power speed characteristic (tracking characteristic) [10,11]. The control system is presented in Fig. 4b.

The grid-side converter (GSC) is utilized to regulate the DC bus capacitor voltage. The control system is depicted in Fig. 4c [10,11]. The grid-side converter control feeds the DC voltage regulator from the difference between V_{dc} and V_{dc} reference, and transfers it into the d-q

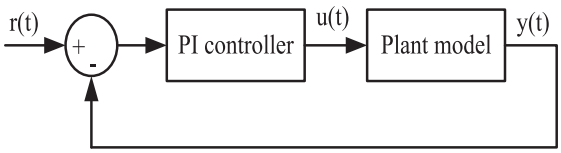

(a). A typical PI controls structure

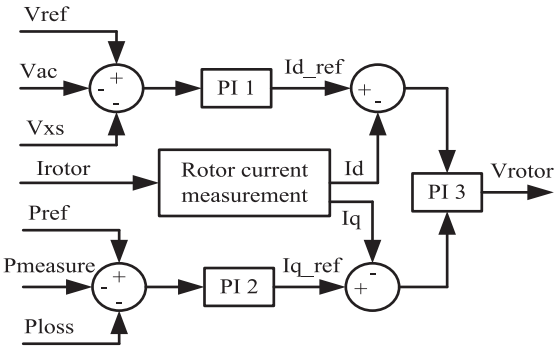

(b). Schematic diagram of RSC

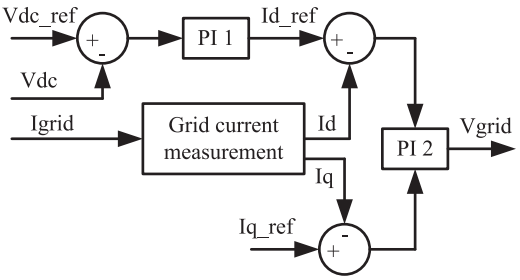

(c). Schematic diagram of GSC

Fig. 4. Controllers structure.

axis current or the current regulator by the PI controller. Then, using the PI controller, it transfers the regulator again into the d-q axis voltage with the electrical equation of Park's transformation. It converts not unlike the rotor-side convertor into using the DFIG controlled. The PI controller is controlled at the optimum point for the DFIG systems.

The complete explanations as wekk as wind speed model and pitch controllers were explained in [11].

Because of the limited reactive power capability, DFIG cannot always supply the required reactive power; as a result, its terminal voltage fluctuates. Therefore, a voltage regulation device is required for the secure operation of the overall wind turbine together with the power grid during normal operation as well as disturbances in the grid [9–12].

According to the new grid codes, WTs must remain connected to the grid and supply reactive power to guarantee the grid voltage during grid faults. This ability of WTs is called the fault ride through (FRT) capability and, for voltage dips, the LVRT capability [39,40]. LVRT depends on the magnitude of voltage drop at the point of common coupling (PCC) during fault and the time taken by the grid system to recover to the normal state [39].

A summary of the voltage profile for ride-through capabilities in the grid codes is presented in Fig. 5 [40]. Only when the grid voltage goes below the curves are the turbines allowed to be disconnected. Moreover, when the voltage is in the special area, the turbines should supply reactive power.

On the other hand, faults in the power system, even far away from the location of the turbine, can cause a voltage dip at the connection point of the wind turbine. The dip in the grid voltage will result in an

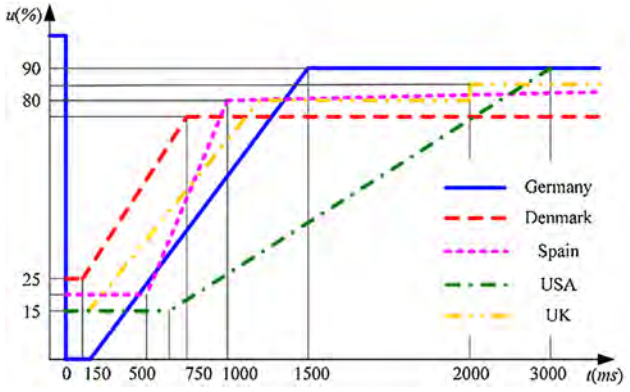

Fig. 5. Voltage profile for LVRT in different countries.

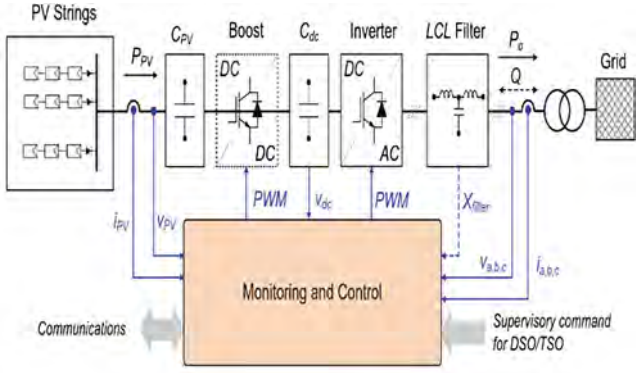

a. Schematic and control function blocks of a typical PV system

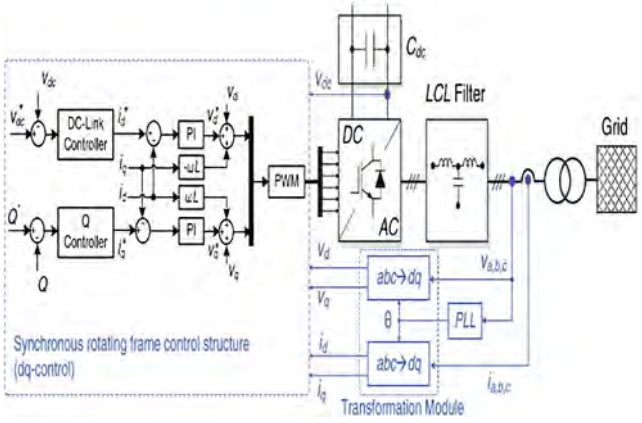

b. General control structure of a three-phase PV inverter

Fig. 6. PV plant.

increase of the current in the stator windings of the DFIG. Because of the magnetic coupling between stator and rotor, this current will also flow into the rotor circuit and power converters, so that it will cause an overcurrent in rotor windings and overvoltage in the DC bus of power converters [10,11]. Without any protection, this will lead to the destruction of converters. In this paper, the proposed solution involves the use of PI controllers and FACTS devices.

3.2. Photovoltaic solar plant

Fig. 6a illustrates the general structure of a three-phase PV system with power feed-in functions [6,7]. The boost stage functions as the input power control stage to extract maximum power from PV strings in normal operation. The control of the grid-side converter (three-phase PV inverter) is normally implemented by regulating the DC-link voltage

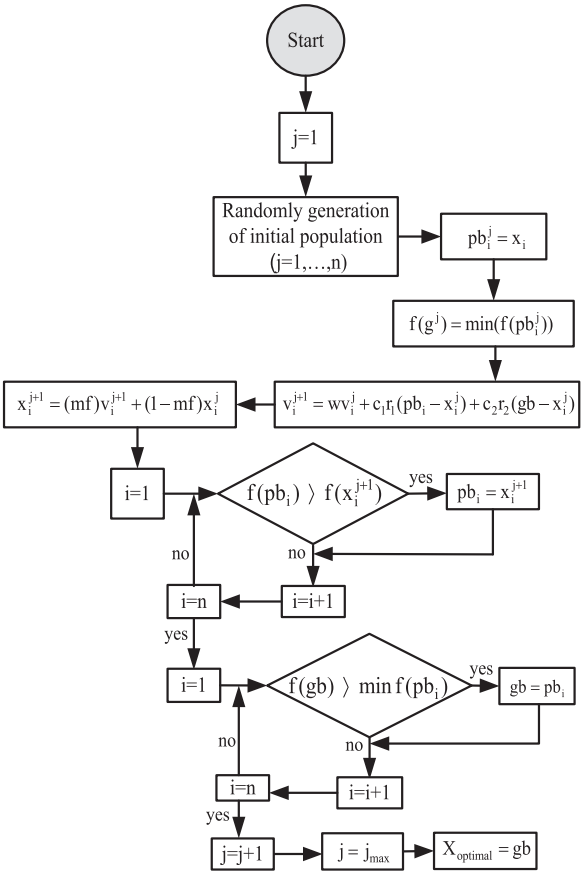

(a). Flowchart of the AVURPSO algorithm

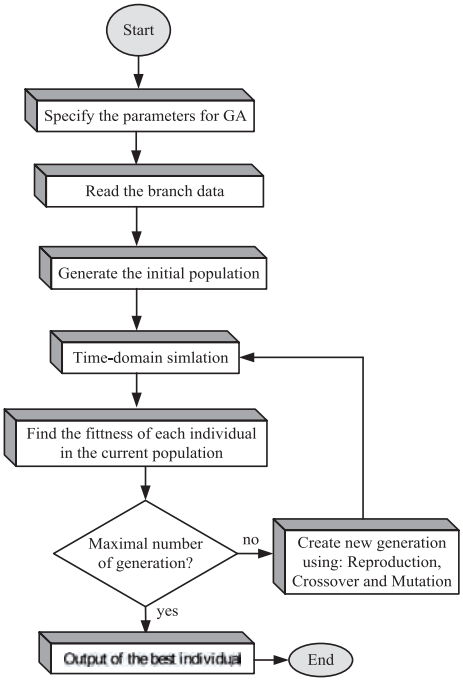

(b). Flowchart of the GA

Fig. 7. Flowchart of optimization algorithms.

in order to maintain the power balance between the PV strings and the grid. It also takes care of the power quality of the generated power by controlling the injected grid current. With the help of the instantaneous power theory and Clark and Park transformations [6,41], the

Table 1
The values of optimized parameters of PSS controller.

Parameters	AVURPSO	GSA	GA	Range
K_{PG1} [pu]	32.1	29.6	20.2	20–60
K_{PG2} [pu]	25.1	23.9	22.6	20–60
K_{PG3} [pu]	37.2	34.3	26.7	20–60
K_{PG4} [pu]	31.2	28.1	26.3	20–60
$T_{1PG1} = T_{3PG1}$ [s]	0.47	0.51	0.63	0.01–1
$T_{1PG2} = T_{3PG2}$ [s]	0.48	0.53	0.56	0.01–1
$T_{1PG3} = T_{3PG3}$ [s]	0.44	0.46	0.48	0.01–1
$T_{1PG4} = T_{3PG4}$ [s]	0.41	0.48	0.52	0.01–1
$T_{2PG1} = T_{4PG1}$ [s]	0.34	0.39	0.43	0.01–1
$T_{2PG2} = T_{4PG2}$ [s]	0.37	0.42	0.46	0.01–1
$T_{2PG3} = T_{4PG3}$ [s]	0.35	0.41	0.44	0.01–1
$T_{2PG4} = T_{4PG4}$ [s]	0.42	0.54	0.62	0.01–1

Table 2
The values of FACTS controllers with AVURPSO.

Parameters	SSSC	Statcom	TCSC	Range
K [pu]	12.3	19.2	29.6	1–50
T_1 [s]	0.36	0.42	0.69	0.01–1
T_2 [s]	0.23	0.25	0.32	0.01–1
T_3 [s]	0.38	0.43	0.58	0.01–1
T_4 [s]	0.28	0.3	0.39	0.01–1

Table 3
The values of FACTS controllers with GSA.

Parameters	SSSC	Statcom	TCSC	Range
K [pu]	14.6	21.3	32.1	1–50
T_1 [s]	0.38	0.48	0.73	0.01–1
T_2 [s]	0.31	0.29	0.35	0.01–1
T_3 [s]	0.4	0.48	0.64	0.01–1
T_4 [s]	0.32	0.34	0.42	0.01–1

Table 4
The values of FACTS controllers with GA.

Parameters	SSSC	Statcom	TCSC	Range
K [pu]	17.1	23.2	35.7	1–50
T_1 [s]	0.4	0.61	0.79	0.01–1
T_2 [s]	0.39	0.32	0.36	0.01–1
T_3 [s]	0.42	0.52	0.71	0.01–1
T_4 [s]	0.38	0.39	0.48	0.01–1

Table 5
The values of optimized parameters of RSC controllers.

Parameters	AVURPSO	GSA	GA
K_{P1} [pu]	8.9	14.7	25.09
K_{I1} [pu]	151.2	168.6	189.3
K_{P2} [pu]	14.6	24.3	35.9
K_{I2} [pu]	98.3	114.3	132.4
K_{P3} [pu]	17.3	25.9	51.3
K_{I3} [pu]	102.7	124.8	155.9

Table 6
The values of optimized parameters of GSC controllers.

Parameters	AVURPSO	GSA	GA
K_{P1} [pu]	7.2	13.6	29.7
K_{I1} [pu]	142.3	159.3	192.3
K_{P2} [pu]	16.5	23.8	17.3
K_{I2} [pu]	99.8	117.1	164.3

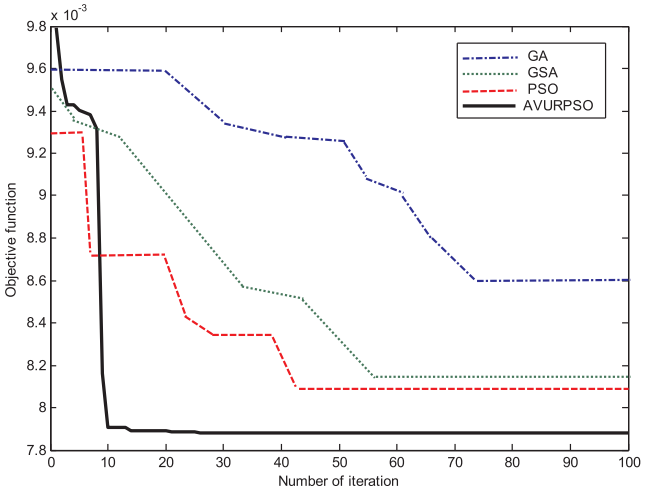

Fig. 8. Convergence of the objective function for gbest.

synchronization and control of three-phase PV inverters are easier than that of single-phase PV inverters.

Applying the Park transformation to a three-phase variable (vabc, iabc) leads to the possibility of dq-control for a three-phase system. This control utilizes the reference frame transformation module (abc to dq) to transform the grid voltage and current waveforms into a reference frame which rotates synchronously with the grid voltage. Consequently, the control variables become DC quantities. Since every deviation of the grid voltage and/or grid current will be reflected to the corresponding d- and q-axis components, it leads to an easy solution for filtering and control by means of PI-based controllers [6,7].

Fig. 6b represents the schematic view of the dq-control for a three-phase PV inverter [6,7]. In this structure, the DC-link voltage is controlled in accordance with the necessary output power. Its output is then utilized as the reference for the active current controller, whereas the reactive current reference is usually set to zero in normal operation. When the reactive power has to be controlled in some cases, a reactive power reference must be imposed on the control system. Since grid currents are required to be synchronized with the grid voltage, a phase-locked loop (PLL) system is also included in this control structure which also provides the grid phase angle, necessary for the Park transformation model (abc to dq). In this paper, AVURPSO, GSA, and GA are utilized to design and optimize the parameters of PI controllers. During fault, the PV system is required to supply a reactive current to enhance grid stability based on the grid code of the PV system [6,41].

4. Optimizing the parameters of SSSC, TCSC, STATCOM and PSS controllers

To optimize the controllers' parameters, an eigenvalue-based objective function is considered. The objective function can be defined as:

$$J = \sum \int_0^{t_1} t\ |\Delta\omega(t, X)|\ dt \tag{23}$$

where Δω(t,X) is the speed deviation of the generator for parameters of SSSC, TCSC, STATCOM, and PSS controllers, and X is the optimization parameters of this controllers. In this study, the objective function is to minimize the proposed objective function J. The introduced approach employs AVURPSO, GSA, and GA to solve this optimization problem and search for the optimal set of controllers' parameters.

4.1. AVURPSO algorithm

The novelty of the present study is finding the global optimum of the spread factor parameter at the upper level using an adaptive velocity update PSO, namely AVURPSO, that has a higher convergence

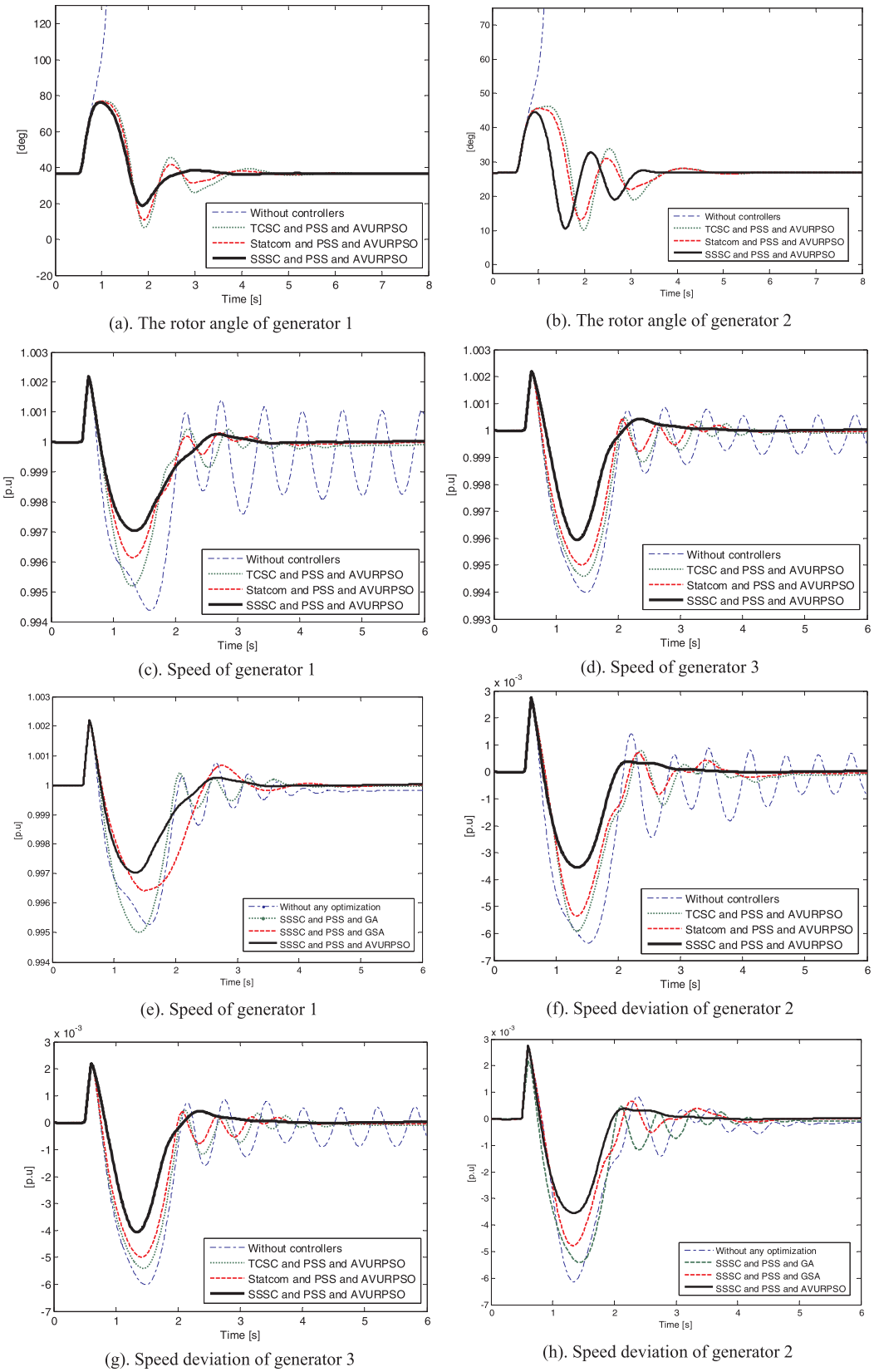

Fig. 9. Simulation results of power system.

speed and accurate response compared to the PSO algorithm. The PSO algorithm is a population-based search algorithm based on the simulation of the social behavior of birds. In the basic PSO algorithm, individuals are referred to as particles. The position of particles within the search space is changed based on the social-psychological tendency of individuals in order to delete other individuals. Namely, the velocity (v) and position (x) of each particle will be changed by the particle best value (pb) and global best value (gb). The velocity and position

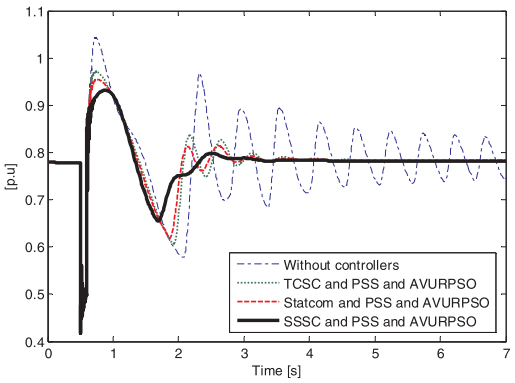

(i). Output power of generator 1

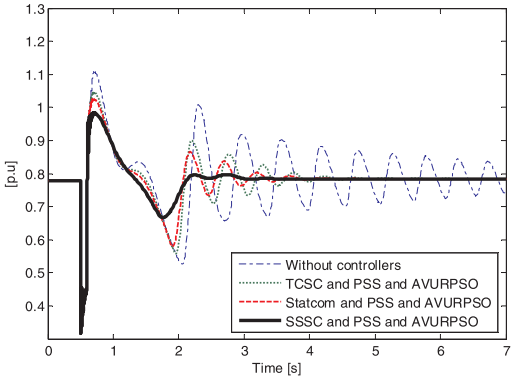

(j). Output power of generator 3

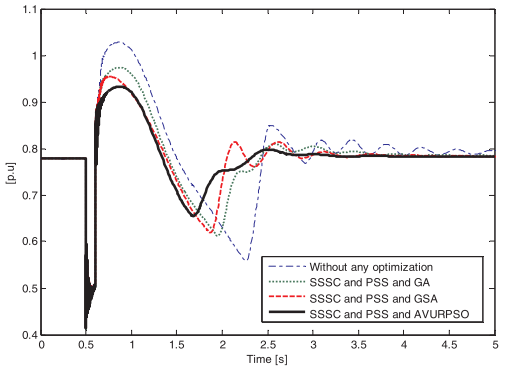

(k). Output power of generator 1

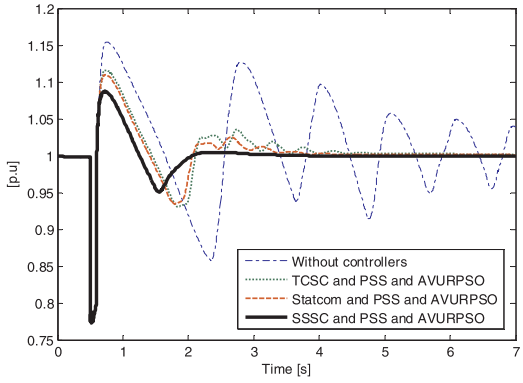

(l). Voltage of bus 10

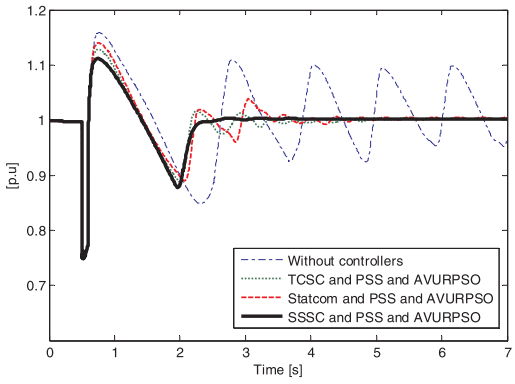

(m). Voltage of bus 13

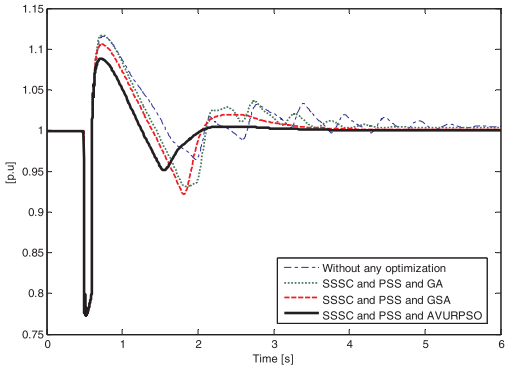

(n). Voltage of bus 10

Fig. 9. (*continued*)

updating of the particle is shown by the following expression:

$$v_i^{j+1} = wv_i^j + c_1 r_1 (pb_i - x_i^j) + c_2 r_2 (gb - x_i^j) \tag{24}$$

$$x_i^{j+1} = v_i^{j+1} + x_i^j \tag{25}$$

where v_i^{j+1} is the velocities of particle i at iterations j, and x_i^{j+1} is the positions of particle i^{th} at iterations j^{th}. Moreover, w is the inertia weight to be employed to control the impact of the previous history of velocities, t denotes the iteration number, c_1 is the cognition learning factor, c_2 is the social learning factor, and r_1 and r_2 are random numbers uniformly distributed in [0, 1]. Generally, the value of each component in v can be clamped to the range $[v_{min}, v_{max}]$ to control the excessive roaming of particles outside the search space.

In traditional PSO, the velocities of particles are limited in the range of $[v_{min}, v_{max}]$. Usually, v_{min} and v_{max} are set to x_{min} and x_{max}, respectively. The positions of particles are given in the range of $[x_{min}, x_{max}]$. Thus, evaluating the results according to the limits for confining or rejecting the results imposes an extra computational burden. AVURPSO postulates boundary velocity validity checking without checking the validity of positions in every iteration cycle [36].

In traditional PSO algorithms, velocity is updated at every iteration cycle. In contrast, in AVURPSO, the velocity of each particle is kept unchanged if its fitness at the current iteration is superior to one at the preceding iteration; otherwise, the particles' velocity is updated as stated by (24) and, as a result, computational efficiency is enhanced. The new position of the particle is then calculated as [36]:

$$x_i^{j+1} = (mf)v_i^{j+1} + (1 - mf)x_i^j \tag{26}$$

Adopting small values for c_1 and c_2 allows the particle to roam far from the target regions before being tugged back. On the other hand, adopting high values results in an abrupt movement forward or passes the target regions. Therefore, c_1 and c_2 are introduced as [36]:

$$c_1 = \frac{(iter_{max} - iter) \times (c_{1b} - c_{1a})}{iter_{max}} + c_{1a} \tag{27}$$

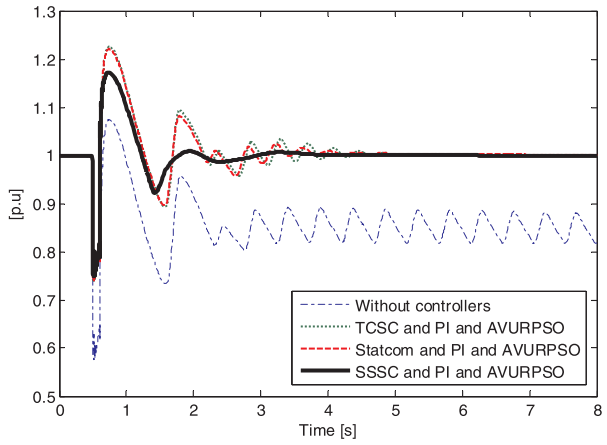

(a). Terminal voltage of DFIG 2

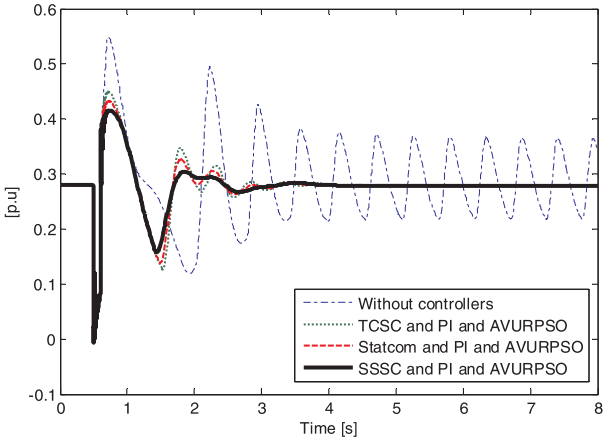

(b). Output active power of DFIG 1

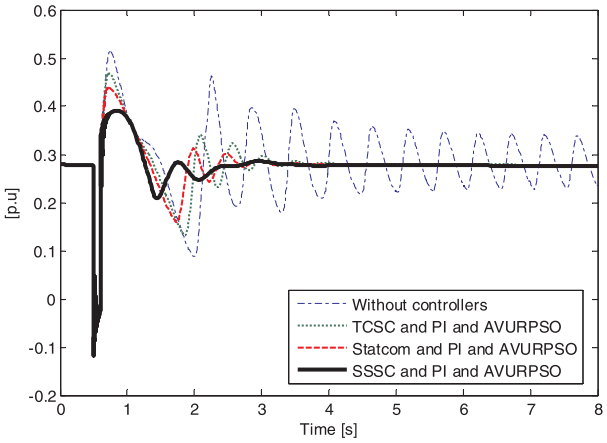

(c). Output active power of DFIG 2

Fig. 10. Simulation results of wind farms.

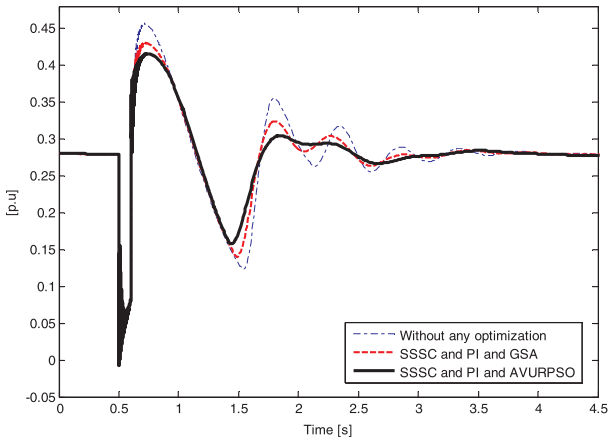

(d). Output active power of DFIG 1

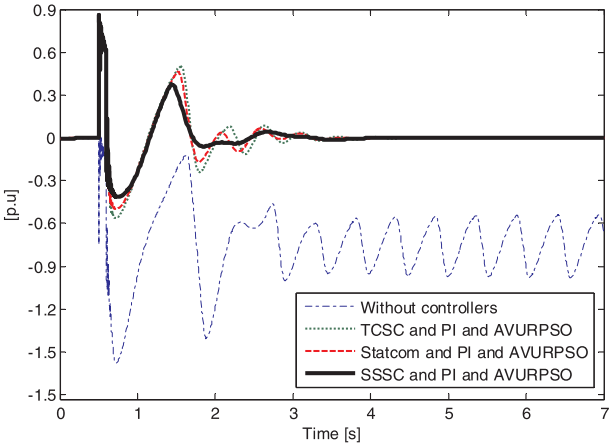

(e). Output reactive power of DFIG 1

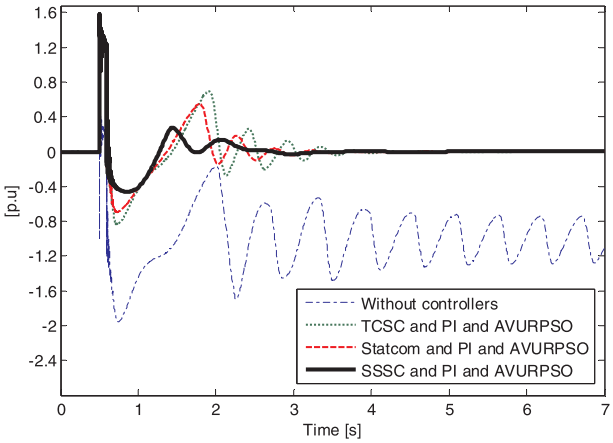

(f). Output reactive power of DFIG 2

Fig. 10. (*continued*)

$$c_2 = \frac{(iter_{\max} - iter) \times (c_{2b} - c_{2a})}{iter_{\max}} + c_{2a} \tag{28}$$

where c_{1b} and c_{2b} are the initial values of c_1 and c_2, and c_{1a} and c_{2a} are the final values of c_1 and c_2, respectively. In fact, the best solutions are determined over the full range of search for changing c_1 from 2.5 to 0.5 and c_2 from 0.5 to 2.5. With a large value of c_1 and a small value of c_2 at the beginning, particles are allowed to move around the search space instead of moving toward the pbesti. A small value of c_1 and a large value of c_2 allow the particles to converge to the gbesti in the latter part of optimization. mf is the momentum factor between 0 and 1. The momentum factor is adaptively changed as follows [36]:

$$mf = \frac{(iter_{\max} - iter) \times (mf_2 - mf_1)}{iter_{\max}} + mf_1 \tag{29}$$

where mf is decreased from a higher value mf1 to a lower value mf_2. The flowchart of AVURPSO algorithm is presented in Fig. 7a [36].

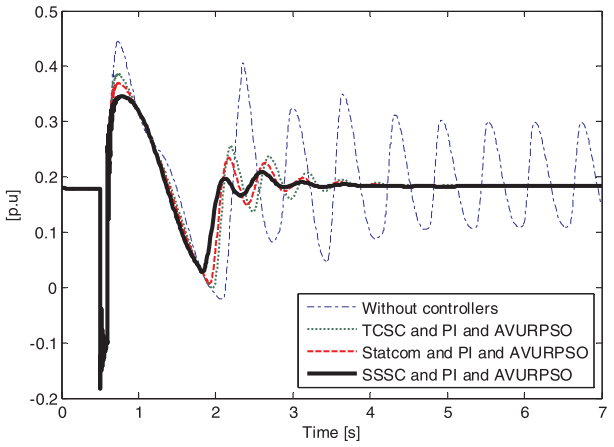

(a). Output active power of PV

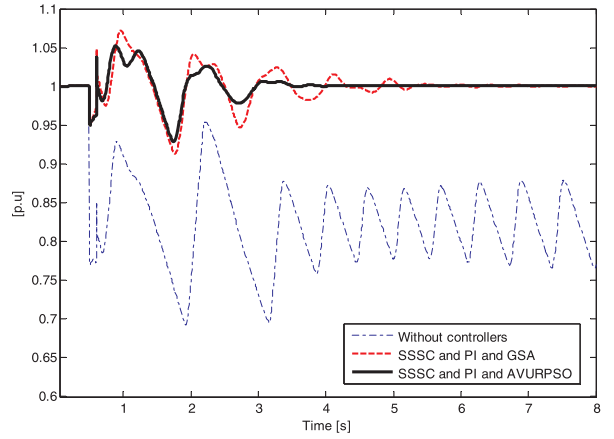

(b). Terminal voltage of PV

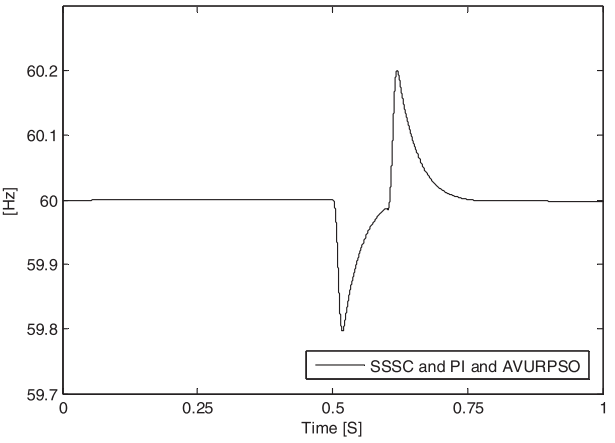

(c). Frequency of bus 13

Fig. 11. Simulation results of the PV plant.

4.2. Genetic algorithm

Genetic algorithms are global search techniques based on the mechanisms of natural selection and genetics. They can simultaneously search several possible solutions and do not require any prior knowledge or special properties of the objective function [30,31]. Moreover, they always produce high-quality solutions and, therefore, are excellent methods for searching for an optimal solution in a complex problem. Particularly in this research, the problem has a very wide range of combinations of solutions, so that it is not feasible to search exhaustively.

Commonly, GAs start with random generation of the initial population which represents possible solutions to the problem. Then, the fitness of each individual is evaluated and new populations are generated by genetic operators (reproduction, crossover, and mutation) until the maximal number of generation is reached. The flowchart of GA is illustrated in Fig. 7b.

4.3. Gravitational search algorithm

The GSA is based on Newton's theory. In GSA, agents are considered as objects and their performance is measured by their masses. All these objects attract one another by the force of gravity, a force which causes a global movement of all objects towards those with a heavier mass. Therefore, masses co-operate using a direct form of communication through gravitational force. The heavy masses which correspond to a good solution move more slowly than lighter ones, thereby guaranteeing the exploitation step of the algorithm [29,34].

In GSA, each mass (agent) has four specifications: position, inertial mass, active gravitational mass, and passive gravitational mass. The position of the mass corresponds to a solution to the problem, and its gravitational and inertial masses are determined using a fitness function. In other words, each mass presents a solution, and the algorithm is navigated by properly adjusting the gravitational and inertial masses. For a system with N-agent (masses), the i^{th} position of an agent X_i is defined by [29,34]:

$$X_i = (X_i^1, ...,X_i^d, ...,X_i^N) \quad For\ i = 1, 2, ...,N \tag{30}$$

At a specific time 't', the force acting on mass 'i' from mass 'j' is defined as follows [29,34]:

$$F_{ij}^d(t) = G(t)\frac{M_{pi}(t) \times M_{aj}(t)}{R_{ij}(t) + \varepsilon}[X_j^d(t) - X_i^d(t)] \tag{31}$$

where M_{aj} represents the active gravitational mass related to agent 'j', M_{pi} denotes the passive gravitational mass related to agent 'i', G(t) indicates the gravitational constant at time 't', and $R_{ij}(t)$ shows the Euclidian distance between two agents 'i' and 'j'. To give a stochastic characteristic to the GSA algorithm, it is assumed that the total force acting on agent 'i' in dimension 'd' is a random weight sum of the 'd'th components of the forces exerted from other agents as [29,34]:

$$F_i^d(t) = \sum_{j=1,j=i}^{N} rand_j F_{ij}^d(t) \tag{32}$$

where rand is a random number in the interval [0, 1]. Furthermore, $a_i^d(t)$ is given as follows:

$$a_i^d(t) = \frac{F_i^d(t)}{M_{ii}(t)} \tag{33}$$

where M_{ii} (t) is the inertia mass of the 'i'th agent. Therefore, its position and velocity can be calculated as follows [29,34]:

$$v_i^d(t + 1) = rand_i \times v_i^d(t) + a_i^d(t) \tag{34}$$

$$x_i^d(t + 1) = x_i^d(t) + v_i^d(t + 1) \tag{35}$$

Gravitational and inertial masses are simply calculated by the fitness evaluation. A heavier mass indicates a more efficient agent, meaning that better agents have a higher attraction and walk more slowly. Assuming the equality of the gravitational and the inertia mass, the values of mass are calculated using the map of fitness. The gravitational and inertial masses are updated by the following equations [29,34]:

$$M_{ai} = M_{pi} = M_{ii} = M_i, \quad i = 1, 2, ...,N \tag{36}$$

$$m_i(t) = \frac{fit_i(t) - worst(t)}{best(t) - worst(t)} \quad (37)$$

$$M_i(t) = m_i(t) / \sum_{j=1}^{N} m_j(t) \quad (38)$$

where $fit_i(t)$ represents the fitness value of the agent 'i' at time 't', and best(t) and worst(t) are defined as follows (for a minimization problem):

$$best(t) = \min fit_j(t) \quad (39)$$

$$worst(t) = \max fit_j(t) \quad (40)$$

Now, the different steps of the GSA algorithm are as follows:

Step 1. Initializing particles in the search space at random
Step 2. Search space identification
Step 3. Randomized initialization
Step 4. Fitness evaluation of agents
Step 5. Updating G(t), best (t), worst (t), and M_i (t) for 1, 2, …., N
Step 6. Calculation of the total force in different directions
Step 7. Calculation of acceleration and velocity
Step 8. Updating the agent's position
Step 9. Repeating Steps 3–8 until the stop criterion is reached

The flowchart of GSA is presented in [29,34].

5. Simulation results

The values for the optimized parameters of PSS are given in Table 1; those for SSSC, TCSC, and STATCOM controllers with AVURPSO algorithm are shown in Table 2; those for GSA are presented in Table 3; and those for GA are listed in Table 4. Also, the values of the optimized parameters of DFIG controllers are given in Tables 5 and 6.

In Fig. 8, the objective function with GA, GSA, PSO, and AVURPSO respectively converges to 0.0086, 0.00818, 0.00814, and 0.00783 for gbest. As a result, the AVURPSO algorithm, in comparison to GA, GSA, and PSO, acts better in minimizing the objective function and, therefore, the gbest of the AVURPSO is superior.

A three-phase line-to-ground fault in line 1 between bus 10 and bus 13 is simulated for 100 ms (Fig. 2). This fault has occurred in 0.5 s and is disappeared in 0.6 s. Several case studies are reported in this paper as given below:

Case study 1. Without controllers
Case study 2. TCSC and PSS simultaneous controllers
Case study 3. STATCOM and PSS simultaneous controllers
Case study 4. SSSC and PSS simultaneous controllers
Case study 5. Review of LVRT in PV and wind farms
Case study 6. Comparison between these four things: without any optimization, AVURPSO, GSA and GA.

As seen in Fig. 9a and b, the rotor angles of generators 1 and 2 are unstable because a three-phase line-to-ground fault has occurred but is damped at about 5.5 s using TCSC and PSS simultaneous controllers and damped shorter than 4.5 s using STATCOM and PSS simultaneous controllers. The duration of damping in about 3.5 s and oscillations step down by the use of SSSC and PSS simultaneous controllers. It demonstrates the superiority and higher speed of SSSC than STATCOM and TCSC.

Considering Fig. 9c and d, the speed of generators 1 and 3 was damped and stabilized using SSSC and PSS simultaneous controllers at about 3.5 s. In Fig. 9e, using the AVURPSO algorithm, oscillation and time damping have been decreased in comparison to GSA and GA. In Fig. 9f–h, the speed deviations of generators 2 and 3 are damped in about 3.5 s by SSSC and PSS simultaneous controllers. Fig. 9i–k indicates the very oscillatory output power of generators 1 and 3, but they are damped in about 3.5 s at an amount before the fault using SSSC and PSS simultaneous controllers.

The voltages of buses 10 and 13 (Fig. 9l and m) are very oscillatory, and the oscillations by SSSC and PSS simultaneous controllers are damped in about 2.1 s at 1 pu. In Fig. 9n, the voltage of bus 10 damped at about 5 s using GA and at about 4 s by GSA. The duration of damping is shorter than 2.1 s, and the oscillations step down by AVURPSO.

The responses of the terminal voltage (PCC), active and reactive power of DFIG1 and 2, are presented in Fig. 10a–f, respectively. The voltage diped during the fault, where voltage can be significantly retained to around 1 pu using PI and FACTS controllers after clearing the fault. It is clear that, from among the described methods, the performance of the SSSC is the best and can effectively stabilize the wind generator system. Considering Figs. 5 and 10a, without controllers, voltage collapse has occurred in the weak-grid condition and the LVRT grid code cannot be satisfied as the wind turbines have to be disconnected from the grid.

The active power, terminal voltage (PCC), and frequency of the PV plant are also depicted in Fig. 11a–c, respectively. As seen in Fig. 11b, voltage can be significantly retained to around 1 pu using PI and FACTS controllers after clearing the fault.

6. Conclusion

In this paper, the power system stability enhancement via PI controllers and PSS and FACTS-based stabilizers when applied through coordinated application was discussed and investigated for a multimachine power system in the presence of PV and wind farms. Parameters of the proposed FACTS, PSS, and PI controllers were optimized using AVURPSO, GSA and GA. The effectiveness of the proposed control schemes in improving the power system transient stability has been verified through eigenvalue analysis and nonlinear time-domain simulations under a three-phase line-to-ground fault.

The system has become unstable following the three-phase line-to-ground fault; however, by the simultaneous application of TCSC and PSS controllers and STATCOM and PSS controllers, the stability of the system improves and its oscillations are damped. Using SSSC and PSS simultaneous controllers, oscillation and time damping have been decreased compared to STATCOM and TCSC. Furthermore, the comparison of the simulated methods indicated that SSSC and PI controllers are the most reliable and effective LVRT capability-enhancement methods for wind and PV farms. Moreover, using the AVURPSO algorithm, oscillation and time damping have been decreased in comparison to GSA and GA. As a result, the performance of the AVURPSO algorithm is superior to that of GSA and GA.

Appendix A. Supplementary material

Supplementary data to this article can be found online at https://doi.org/10.1016/j.ijepes.2018.10.019.

References

[1] Cao Y, Zhang Y, Shi X. Probabilistic optimal PV Capacity planning for wind farm expansion based on NASA data. IEEE Trans Sustain Energy 2017;8(March):1291–300.
[2] Jalilian A, Naderi SB. Low voltage ride-through enhancement of DFIG-based wind turbine using DC link switchable resistive type fault current limiter. Electr Power Energy Syst 2017;86(March):104–19.
[3] Chowdhury MA, Sayem AH. Robust active disturbance rejection controller design to improve low-voltage ride-through capability of doubly fed induction generator wind farms. IET Renew Power Gener 2015;9(November):961–9.
[4] Abdou A, Abu-Siada A. Impact of VSC faults on dynamic performance and low voltage ride through of DFIG. Electr Power Energy Syst 2015;65(February):334–47.
[5] Long T, Shao S, Abdi E. Asymmetrical low-voltage ride through of brushless doubly fed induction generators for the wind power generation. IEEE Trans Energy Convers 2013;28(June):502–11.
[6] Wang L, Quang-Son V. Stability improvement of a multimachine power system

connected with a largescale hybrid wind-photovoltaic farm using a supercapacitor. IEEE Trans Ind Appl 2017(September):521–68.
[7] Hossain M, Hasan Ali M. Fuzzy logic controlled power balancing for low voltage ride-through capability enhancement of large-scale grid-connected PV plants. In: IEEE/TPEC, March 2017. p. 1–6.
[8] Ahmed AA, Abdelsalam HA. Mitigation of transformer-energizing inrush current using grid-connected photovoltaic system. Electr Power Energy Syst 2016;79(July):312–21.
[9] Jiabing Hu, Nian Heng. Dynamic modeling and improved control of DFIG under distorted grid voltage conditions. IEEE Trans Energy Convers 2011;26(March):163–75.
[10] Tang Y, He Haibo. Power system stability control for a wind farm based on adaptive dynamic programming. IEEE Trans Smart Grid 2015;6(January):166–77.
[11] Pokharel B. Modeling, control and analysis of a doubly fed induction generator based wind turbine system with voltage regulation. Master of science electrical engineering tennessee technological university, December 2011.
[12] Geng H, Yang G. Small-signal stability of power system integrated with ancillary-controlled large-scale DFIG-based wind farm. IET Renew Power Gener 2017;11(July):1191–8.
[13] Ghahremani E, Kamwa I. Analysing the effects of different types of FACTS devices on the steady-state performance of the Hydro-Québec network. IET Gener Transm Distrib 2014;8(February):233–49.
[14] Samantaray SR. Decision tree-based fault zone identification and fault classification in flexible AC transmissions-based transmission line. IET Gener Transm Distrib 2009;3(May):425–36.
[15] Nguyen-Duc H, Dessaint L, Okou AF, Kamwa I. A power oscillation damping control scheme based on bang-bang modulation of FACTS signals. IEEE Trans Pow Sys 2010;25(4):1918–27.
[16] Ford JJ, Ledwich G. Efficient and robust model predictive control for first swing transient stability of power systems using flexible AC transmission systems devices. IET Gener Transm Distrib 2008;2(July):731–42.
[17] Thirumalaivasan R. Damping of SSR using subsynchronous current suppressor with SSSC. IEEE Power Energy Soc 2013;28:64–74.
[18] Ankitkumar B. A SSSC based damping controller for stability enhancement of power system. In: IEEE/AEEICB, February 2017. p. 183–7.
[19] Eremia M, Liu Chen-Ching. Static synchronous series compensator (SSSC). Wiley-IEEE Press eBook Chapters; 2016.
[20] Abapour M, Aliasghari P. Risk-based placement of TCSC for transient stability enhancement. IET Gener Transm Distrib 2016;10(October):3296–303.
[21] Yang R, Hug-Glanzmann G. Regression-based control of thyristor-controlled series compensators for optimal usage of transmission capacity. IET Gener Transm Distrib 2014;8(8):1444–52.
[22] Wang L, Chang C. Stability improvement of a two-area power system connected with an integrated onshoreo and offshore wind farm using a STATCOM. IEEE Ind Appl Soc 2016;53(November):867–77.
[23] He Zhixing, Ma Fujun, Qianming Xu. Reactive power strategy of cascaded delta-connected statcom under asymmetrical voltage conditions. IEEE J Emerg Selec Top Power Electron 2017;5(June):784–95.
[24] Dysko E, Leithead WE. Enhanced power system stability by coordinated PSS design. IEEE Trans Power Syst 2010;25(February):413–42.
[25] Bian XY, Geng Yan, Lo Kwok L. Coordination of PSSs and SVC damping controller to improve probabilistic small-signal stability of power system with wind farm integration. IEEE Trans Power Syst 2016;31(May):2371–82.
[26] Hasanvand H, Arvan MR. Coordinated design of PSS and TCSC to mitigate interarea oscillations. Int J Electr Power Energy Syst 2016;78(June):194–206.
[27] Jordehi AR. Brainstorm optimisation algorithm (BSOA): An efficient algorithm for finding optimal location and setting of FACTS devices in electric power systems. Int J Electr Power Energy Syst 2015;69(July):48–57.
[28] Wang L, Truong D. Stability enhancement of a power system with a PMSG-based and a DFIG-based offshore wind farm using a SVC with an adaptive-network-based fuzzy inference system. IEEE Trans Ind Electron 2013;60(July):2799–807.
[29] Sarker J, Goswami SK. Solution of multiple UPFC placement problems using gravitational search algorithm. Int J Electr Power Energy Syst 2014;55(February):531–41.
[30] Hassan LH, Moghavvemi M. Application of genetic algorithm in optimization of unified power flow controller parameters and its location in the power system network. Int J Electr Power Energy Syst 2013;46(March):89–97.
[31] Hassan LH, Moghavvemi M. A coordinated design of PSSs and UPFC-based stabilizer using genetic algorithm. IEEE Trans Ind Appl 2014;50(October):2957–66.
[32] Ravi K, Rajaram M. Optimal location of FACTS devices using improved particle swarm optimization. Int J Electr Power Energy Syst 2013;49(July):333–8.
[33] Al-Awami AT, Abdel-Magid YL. A particle-swarm-based approach of power system stability enhancement with unified power flow controller. Int J Electr Power Energy Syst 2007;29(March):251–9.
[34] Abd Elazim SM, Ali ES. Optimal SSSC design for damping power systems oscillations via gravitational search algorithm. Int J Electr Power Energy Syst 2016;82(November):161–8.
[35] Bhattacharyya B, Kumar S. Approach for the solution of transmission congestion with multi-type FACTS devices. IET Gener Transm Distrib 2016;10(August):2802–9.
[36] Shahgholian G, Movahedi A. Power system stabiliser and flexible alternating current transmission systems controller coordinated design using adaptive velocity update relaxation particle swarm optimisation algorithm in multi-machine power system. IET Gener Transm Distrib 2016;10(May):1860–8.
[37] Zirkohi MM, Fateh MM. Design of radial basis function network using adaptive particle swarm optimization and orthogonal least squares. J Software Eng Appl 2010;3(July):704–8.
[38] Saleh MB, Abido MA. Power system damping enhancement via coordinated design of PSS and TCSC in multi-machine power system. In: IEEE/GCC, March 2006. p. 1–6.
[39] Geng H, Liu C, Yang G. LVRT capability of DFIG-based WECS under asymmetrical grid fault condition. IEEE Trans Ind Electron 2013;60(6).
[40] Tsili M, Papathanassiou S. “A review of grid code technical requirements for wind farms”, chool of Electrical and Computer Engineering, National Technical University of Athens (NTUA); 2009. p. 308–12.
[41] Teodorescu R, Liserre M, Rodriguez P. Grid converters for photovoltaic and wind power systems. IEEE J Mag 2011.